Modeling the Transfer Function of Two-Dimensional SQUID and SQIF Arrays with Thermal Noise

M.A. Galí Labarias,* K.-H. Müller, and E.E. Mitchell
CSIRO Manufacturing, Lindfield, New South Wales, 2070, Australia

(Received 20 June 2021; revised 18 November 2021; accepted 22 April 2022; published 3 June 2022)

We present a theoretical model for two-dimensional (2D) superconducting quantum interference device (SQUID) and superconducting quantum interference filter (SQIF) arrays with overdamped Josephson junctions for uniform bias-current injection at 77 K. Our simulations demonstrate the importance of including Johnson thermal noise and reveal that only the SQUID-loops self-inductance contributions are of importance. Our numerical results establish the validity of a scaling behavior between the voltages of one-dimensional (1D) and 2D SQUID arrays and show that the same scaling behavior applies to the maximum transfer functions. The maximum transfer function of a 2D SQUID array can be further optimized by applying the optimal bias current, which depends on the SQUID-loop self-inductance and the junction critical current. Our investigation further reveals that a scaling behavior exists between the maximum transfer function of a 2D SQUID array and that of a single dc SQUID. Finally, we investigate the voltage response of 1D and 2D SQIF arrays and illustrate the effects of adding spreads in the heights and widths of SQUID loops.

DOI: 10.1103/PhysRevApplied.17.064009

I. INTRODUCTION

Superconducting quantum interference devices (SQUIDs) have been extensively investigated for their very high magnetic field sensitivity both experimentally and theoretically [1,2]. SQUIDs are routinely fabricated using both low-temperature-superconducting (LTS) and high-temperature-superconducting (HTS) thin films. The lower operating temperature provides LTS SQUIDs with better noise performance at the expense of more complex cryogenic conditions, compared to HTS SQUIDs. For example, HTS SQUIDs have found applications in geophysical exploration [3], due to less stringent cryogenic constraints resulting in SQUID systems with reduced size, weight, and power. Ambegaokar and Halperin [4] and Voss [5] have studied the effect of thermal noise on the I-V characteristics of shunted Josephson junctions (JJs) and Tesche and Clarke [6] and Enpuku *et al.* [7] have extensively investigated the effect of thermal noise on the performance of dc SQUIDs. These studies show a significant decrease in the voltage-modulation depth and transfer function due to thermal noise at high temperatures (77 K).

The interest in SQUID arrays have arisen in order to improve the sensitivity and robustness of dc SQUIDs. Miller *et al.* [8] have theoretically studied one-dimensional (1D) SQUID arrays, also called superconducting quantum interference gratings (SQUIGs), as an analogy to optical interference gratings. In that work, the authors have considered self- and mutual-inductance effects of SQUIDs connected in parallel, as well as different screening parameters. Their results predict a better magnetic field resolution for 1D parallel SQUID arrays compared to a single dc SQUID. Despite this prediction, Gerdemann *et al.* [9] has experimentally measured small 1D parallel arrays of HTS SQUIDs, showing a decrease of the voltage modulation, which has been attributed to bias-current-induced magnetic flux. Likewise, Mitchell *et al.* [10] have experimentally found a degradation in the voltage modulation with the number N of junctions in parallel for $N > 11$ and modeling has predicted either a plateau or a decrease of the transfer function with N, depending on the bias-current lead configuration. Early measurements of 1D arrays of M SQUIDs connected in series [11,12] have shown voltage-modulation improvement and white-noise reduction with increasing M.

Superconducting quantum interference filters (SQIFs) have been theoretically proposed [13,14] and experimentally demonstrated [15–17] by the Schopohl group. The SQUIDs making up these arrays have different loop areas, creating destructive voltage interference for magnetic fluxes away from zero external magnetic flux. The resulting unique dip in the magnetic-field-to-voltage characteristic makes SQIF arrays ideal to perform absolute magnetic field measurements as well as for other applications that benefit from a unique working point. That is why this concept is used by a growing number of groups

*marc.galilabarias@csiro.au

aiming at its basic properties [18,19] and its applicability in, for example, magnetometry [20–24] and rf electronics [25–27]. SQIFs have been studied and realized in LTS and HTS technologies, where the latter in particular benefit from the superior tolerance of SQIFs against parameter inhomogeneities [20,24,25]. The robustness of these devices also extends to harsh and perturbative environmental conditions [23], which gains importance in the context of the commercialization of systems that are based on these devices. Up to now, several topologies of SQIFs have been reported: 1D parallel arrays [13,15,16,18,24], 1D serial arrays [14,16,22–24], combinations of these two [20,24], and two-dimensional (2D) arrays [17,21]. Interest has grown in the performance of the last of these, which are predicted to be more suitable as plug-in replacements for single SQUIDs than other forms of SQIFs while yielding the improved sensitivity, dynamic range, bandwidth, and linearity of the latter compared with single SQUIDs [24]. Kornev *et al.* [27,28] have studied 1D parallel SQIF arrays connected in series and analyzed the SQUID coupling in the array. They have also shown the linear increase of the voltage modulation with the number of SQIFs in series and the conservation of linearity. An alternative approach has been studied by Longhini *et al.* [29] by varying the distance between the nonlocally coupled SQUIDs. In doing so, the magnetic coupling between SQUIDs differs, which breaks the periodicity of the voltage with the applied magnetic field.

One-dimensional parallel SQUID and SQIF arrays have been previously theoretically studied at $T = 0K$ [10,30,31] and experimentally investigated at high temperatures ($T = 77K$) [10]. Recently, Müller and Mitchell [32] have introduced a theoretical model for 1D parallel HTS SQUID arrays that includes thermal noise and fluxoid focusing. This model shows excellent agreement with experimental results at 77 K.

Large 2D SQUID arrays operating at high temperatures have been experimentally measured and studied [33,34]. Two-dimensional SQUID arrays models without considering thermal noise have been previously investigated by Cybart *et al.* [35], Dalichaouch *et al.* [36], and Taylor *et al.* [34] but these models become inaccurate at 77 K, where the thermal-noise strength is large.

The goal of this work is to investigate the scaling behavior between a 2D SQUID array and its 1D-array row components and dc-SQUID cells. To do so, we introduce a model that accurately calculates the response of 2D SQUID and SQIF arrays operating at finite temperature by including the thermal noise from the junction resistors. Our theoretical model assumes overdamped junctions [the resistively shunted junction (RSJ) model] and short junctions, i.e., the junction width w is smaller than the Josephson penetration depth λ_J [37]. The model also includes the magnetic flux coupling due to all the currents flowing in the array as well as the magnetic flux created by the bias leads. The conservation of currents at every vertex of the array is taken into account. We assume that the superconducting tracks and leads that form the SQUID or SQIF arrays are in the Meissner state. In this work, we demonstrate that the inclusion of thermal noise is crucial to obtain the correct array response for devices operating at high-temperatures (77 K), where thermal noise plays an important role. We use this model to compare the time-averaged voltage and the maximum transfer function of 1D and 2D SQUID arrays at $T = 77$ K for different bias currents. We show that the array partial inductances that do not belong to the self-inductances are of minor importance in calculating the maximum transfer function and the overall voltage response. Most importantly, we demonstrate that the voltage response of 1D and 2D SQUID arrays is approximately proportional to the number of loops or rows connected in series and that the maximum transfer function of a 2D SQUID array can be directly related to the maximum transfer function of a dc SQUID. These scaling approximations are more accurate at bias currents close to the optimal one. Furthermore, we compare 2D SQIF arrays with different SQUID area distributions.

Our paper is structured as follows. In Sec. II, we introduce the mathematical framework of our model for 2D SQUID and SQIF arrays. We derive the system of coupled differential equations for the phase differences of the overdamped JJs of the array, where we include the effects of the partial inductances of the whole device and the Johnson thermal noise from the JJ resistors. In Sec. III, we present our simulation results. In Sec. III A, we emphasize the importance of thermal noise and in Sec. III B we study the voltage response of 2D SQUID arrays and the effect of considering the partial inductances of the whole array versus only considering the self-inductances of the SQUID loops. In Sec. III C, we investigate the dependence of the maximum transfer function on the device bias current and array size, while in Sec. III D we reveal its dependence on the JJ critical current and the SQUID-loop self-inductance. In Sec.III E, we show how the maximum transfer function of a 2D SQUID array is related to that of a dc SQUID. In Sec. III F, we discuss the voltage-modulation depth of 2D SQUID arrays. In Sec. III G, we present our findings for 2D SQIF arrays. Finally, in Sec. IV, we give a summary of our work.

II. MATHEMATICAL MODEL

In Fig. 1, we show a schematic diagram of the 2D SQUID and SQIF arrays under study, which consist of SQUIDs connected by sharing JJs along their sides. The loop areas are identical for SQUID arrays while they differ for SQIF arrays. We use the notation (N_s, N_p) array, which is an array with N_s JJs in series and N_p JJs in parallel. The $(1, 2)$ array is the common dc SQUID, a 1D parallel array is a $(1, N_p)$ array, and a serial dc-SQUID array is a

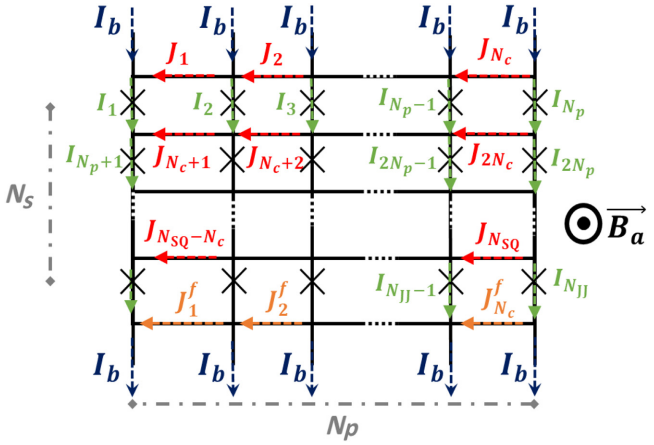

FIG. 1. A diagram of the different currents used in our model for SQUID and SQIF arrays. The arrows indicate the current direction used for Kirchhoff's law analysis. In dark blue, we show the time-independent bias currents I_b. The green arrows represent the vertical currents I_k, which have the same direction as the bias currents. The red arrows depict the horizontal currents J_k and the orange arrows represent the horizontal currents J_k^f flowing along the bottom part of the SQUIDs in the last row. The black crosses indicate JJs. The applied magnetic field $\vec{B}_a$ points upward, perpendicular to the array as indicated. N_p is the number of JJs connected in parallel per row, while N_s is number of rows. Finally, $N_c = N_p - 1$ is the number of SQUIDs in parallel (the number of columns).

$(N_s, 2)$ array. These arrays have $N_c = N_p - 1$ SQUIDs in each row, a total number of SQUIDs of $N_{SQ} = N_c \times N_s$, and a total number of JJs of $N_{JJ} = N_p \times N_s$. In this study, we assume a gridlike structure, where the heights of the SQUIDs in the same row are equal. The same holds for the widths of the SQUIDs in the same column. In our arrays, the JJs are located only in the vertical tracks, which is very different from the so-called JJ arrays, where JJs are also present along the horizontal tracks [38].

For this study, we assume uniformly biased arrays, i.e., there are N_p entering and exiting bias leads that carry equal currents I_b (Fig. 1).

As the SQUID loops are rectangular, it is convenient to define vertical currents I_k and horizontal currents J_k (Fig. 1). Assuming identical overdamped JJs (the RSJ model), we derive the current-phase equation

$$I_k(t) + I_k^n(t) = I_c \sin\varphi_k(t) + \frac{\Phi_0}{2\pi R}\frac{d\varphi_k(t)}{dt}, \tag{1}$$

where t is the time, I_c and R are the critical current and normal resistance of the JJs, and Φ_0 the flux quantum. $\varphi_k(t)$ is the time-dependent gauge-invariant phase difference across the kth junction and $I_k^n(t)$ is the noise current created by the Johnson thermal noise at the kth junction.

A. Kirchhoff's law

At each vertex (crossing point between tracks), we can apply Kirchhoff's law, which gives

$$I_k = J_k - J_{k-1} + I_b, \tag{2}$$

$$I_{(n-1)N_p+k} = J_{(n-1)N_c+k} - J_{(n-1)N_c+(k-1)} + I_{(n-2)N_p+k}, \tag{3}$$

with $1 < k < N_p$ and $1 < n \leq N_s$. Here, Eq. (2) corresponds to any inside vertex of the top row and Eq. (3) defines any inside vertex of any other row (i.e. $1 < n \leq N_s$). For the first vertex of each row, we find

$$I_1 = J_1 + I_b, \tag{4}$$

$$I_{(n-1)N_p+1} = J_{(n-1)N_c+1} + I_{(n-2)N_p+1}. \tag{5}$$

Equivalently, for the last vertex of each row, we obtain

$$I_{N_p} = -J_{N_c} + I_b, \tag{6}$$

$$I_{nN_p} = -J_{nN_c} + I_{(n-1)N_p}. \tag{7}$$

Using matrix notation, we can combine Eqs. (2)–(7) and obtain

$$\hat{K}_I\vec{I} = \hat{K}_J\vec{J} + \vec{I}_b, \tag{8}$$

$$\vec{I} = \hat{K}_I^{-1}\left(\hat{K}_J\vec{J} + \vec{I}_b\right), \tag{9}$$

where $\hat{K}_I$ is a square matrix with dimensions $[N_{JJ} \times N_{JJ}]$ and $\hat{K}_J$ is a matrix with dimensions $[N_{JJ} \times N_{SQ}]$. The elements of these two matrices are defined as

$$(\hat{K}_I)_{ij} = \delta_{i,j} - \delta_{i-N_p,j}, \tag{10}$$

$$(\hat{K}_J)_{ij} = \delta_{i,j} - \delta_{i-1,j}, \tag{11}$$

where $\delta_{i,j}$ is the Kronecker delta.

The current vectors are defined as

$$\vec{I} = (I_1, I_2, \ldots, I_{N_{JJ}})^T, \tag{12}$$

$$\vec{J} = (J_1, J_2, \ldots, J_{N_{SQ}})^T, \tag{13}$$

$$\vec{I}_b = (I_b, I_b, \ldots, I_b, 0, \ldots, 0)^T, \tag{14}$$

$$\vec{I}_f = (I_b, I_b, \ldots, I_b)^T, \tag{15}$$

where the superscript T denotes transposition. Note that $\vec{J}$ does not contain the J_k currents of the bottom horizontal tracks. The bias-current vector $\vec{I}_b$ has dimension $[N_{JJ}, 1]$, with the first N_p components equal to I_b and the rest being zero, and the bias-current vector for the leads exiting from the bottom of the array $\vec{I}_f$ has dimension $[N_p, 1]$.

B. Geometric and kinetic inductance

Using the second Ginzburg-Landau equation [39], we can find a relationship between the phases, fluxes, and currents of the array. As we only have JJs on the vertical sides of each loop, we can choose a closed path around each loop that will connect the total magnetic flux threading each SQUID with the phases of its two junctions and we obtain

$$\frac{\Phi_0}{2\pi}\left(\varphi_{k+1}-\varphi_k\right)=\Phi_s^a+\Phi_s^L+\mu_0\lambda^2\oint_{\mathcal{C}_s}\vec{j}\cdot\vec{dl}, \tag{16}$$

where μ_0 is the permeability of vacuum, λ is the London penetration depth [40] of the material, and $\vec{j}$ is the current density along the closed anticlockwise path $\mathcal{C}_s$ that encircles the sth SQUID. Here, $s=k-(n-1)$, where k is the index of the left JJ in the referred SQUID and n is the index of its row. In Eq. (16), Φ_s^a is the applied flux threading the sth SQUID and Φ_s^L is the flux-threading-loop number s generated by all the currents flowing in the array (including the leads). The applied magnetic flux is $\Phi_s^a=B_a\times a_s^x\times a_s^y$, with B_a the perpendicular applied magnetic field (Fig. 1) and a_s^x and a_s^y the width and height of the sth SQUID loop, respectively (Fig. 2).

The flux Φ_s^L can be expressed in terms of the partial geometric inductances (L values) and currents as

$$\Phi_s^L=\underbrace{\sum_n^{N_{\rm JJ}}L_{sn}^v I_n+\sum_n^{N_{\rm SQ}}L_{sn}^H J_n+\sum_n^{Nc}L_{sn}^{hf}J_n^f}_{\text{magnetic flux created by the array tracks}}+\underbrace{I_b\sum_n^{N_p}L_{sn}^b}_{\text{magnetic flux created by the bias leads}}, \tag{17}$$

where L_{sn}^j are the partial-inductance terms, in which the first subscript, s, defines the SQUID loop where the magnetic flux is induced, and the second subscript defines the current creating that flux. The superscript indicates the different superconductor tracks, i.e., vertical (v), horizontal (H), bottom horizontal tracks of the array (hf), and bias leads (b), where $L_{sn}^b=L_{sn}^{\rm in}+L_{sn}^{\rm out}$, in which $L_{sn}^{\rm in}$ and $L_{sn}^{\rm out}$ are the partial inductances of the top and bottom bias leads.

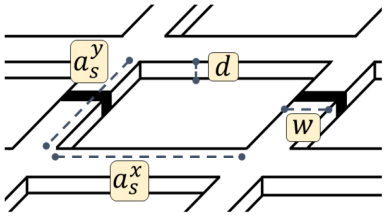

FIG. 2. A sketch of the sth SQUID in the array. a_s^x and a_s^y are the width and height of the sth SQUID loop, w is the track width, and d is the film thickness. The JJs are represented by thick black cuts in the vertical-loop tracks.

Because in our case the Pearl penetration depth [41] $\Lambda=\lambda^2/d$ (d is the film thickness) satisfies $w/2\lesssim\Lambda$, the current density $\vec{j}$ is approximately homogeneous across tracks. Therefore, the last term in Eq. (16) becomes

$$\mu_0\lambda^2\oint_{\mathcal{C}_s}\vec{j}\cdot\vec{dl}=\frac{\mu_0\Lambda}{w}\left(a_s^y\left[I_k-I_{k+1}\right]+a_s^x\left[J_s-J_{s+N_c}\right]\right). \tag{18}$$

The terms $(\mu_0\Lambda/w)a_s^x$ and $(\mu_0\Lambda/w)a_s^y$ are the partial kinetic inductances of the sth SQUID loop. In order to simplify the notation, from this point onward, we incorporate the partial-kinetic-inductance terms into the partial geometric self-inductances in Eq. (17).

Writing Eqs. (16) and (17) in matrix notation, we derive

$$\frac{\Phi_0}{2\pi}\hat{D}\vec{\varphi}=\vec{\Phi}_a+\hat{L}_v\vec{I}+\hat{L}_H\vec{J}+\hat{L}_{hf}\vec{J}_f+\hat{L}_b\vec{I}_b, \tag{19}$$

where $\vec{\varphi}=(\varphi_1,\varphi_2,\ldots,\varphi_{N_{JJs}})^T$ and $\vec{\Phi}_a=(\Phi_1^a,\Phi_2^a,\ldots,\Phi_{N_{\rm SQ}}^a)^T$.

$\hat{D}$ is a matrix of dimensions $[N_{\rm SQ}\times N_{\rm JJ}]$, defined as

$$\hat{D}_{ij}=\delta_{i,j-1}-\delta_{i,j}. \tag{20}$$

C. Phase-difference dynamics of the array

To derive a system of coupled differential equations for the phase differences φ_k that describes the array dynamics, we need to express Eq. (1) in terms of the time-dependent phase differences $\varphi_k(t)$ and time-independent quantities. To achieve this, we start by writing Eq. (19) in terms of the horizontal currents J_k.

We note that the current vector $\vec{J}_f$ (Fig. 1) can be expressed in terms of $\vec{I}$ and $\vec{I}_f$ as

$$\vec{J}_f=\hat{N}_f\vec{I}_f-\hat{N}_I\vec{I}, \tag{21}$$

where the matrices $\hat{N}_f$ and $\hat{N}_I$ ensure conservation of current at the vertices at the bottom part of the array. The dimensions of $\hat{N}_f$ and $\hat{N}_I$ are $[N_c\times N_p]$ and $[N_c\times N_{\rm JJ}]$, respectively, and these matrices are defined as

$$\left(\hat{N}_f\right)_{ij}=\sum_{k=1}^{i}\delta_{k,j}, \tag{22}$$

$$\left(\hat{N}_I\right)_{ij}=\sum_{k=1}^{i}\delta_{N_{JJs}-N_p+k,j}. \tag{23}$$

Using Eqs. (20)–(23), we rewrite Eq. (19) as

$$\frac{\Phi_0}{2\pi}\hat{D}\vec{\varphi} = \vec{\Phi}_a + \hat{L}_V\vec{I} + \hat{L}_H\vec{J} + \hat{L}_b\vec{I}_b + \hat{L}_{hf}\hat{N}_f\vec{I}_f \ , \quad (24)$$

where we define $\hat{L}_V = \left(\hat{L}_v - \hat{L}_{hf}\hat{N}_I\right)$.

Finally, using conservation of currents [see Eq. (9)], we can express the phase-current equation, Eq. (24), in terms of only the $\vec{J}$ currents, which gives

$$\frac{\Phi_0}{2\pi}\hat{D}\vec{\varphi} = \vec{\Phi}_{nf} + \hat{L}\vec{J}, \quad (25)$$

where $\hat{L} = \left(\hat{L}_V\hat{K} + \hat{L}_H\right)$, with $\hat{K} = \hat{K}_I^{-1}\hat{K}_J$, and $\vec{\Phi}_{nf} = \vec{\Phi}_a + \left(\hat{L}_V\hat{K}_I^{-1} + \hat{L}_b\right)\vec{I}_b + \hat{L}_{hf}\hat{N}_f\vec{I}_f$ are time-independent quantities.

The next step is to express Eq. (1) in matrix form, i.e.,

$$\frac{\vec{I}}{I_c} + \vec{i}_n = \overrightarrow{\sin(\varphi(\tau))} + \frac{\overrightarrow{d\varphi(\tau)}}{d\tau}, \quad (26)$$

where $\overrightarrow{\sin\varphi}$ is a vector with components $\sin(\varphi_k)$, $\tau = \omega_c \times t$ is the normalized time, in which $\omega_c = 2\pi RI_c/\Phi_0$ is the characteristic frequency, and $\vec{i}_n = \vec{I}_n/I_c$ is the normalized noise-current vector.

Finally, combining Eqs. (9), (25), and (26), we obtain a coupled system of first-order nonlinear differential equations for $\varphi_k(\tau)$ that describes the time evolution of the array as

$$\frac{\overrightarrow{d\varphi}}{d\tau} = \left[\vec{i}_n - \overrightarrow{\sin(\varphi)} + \frac{\Phi_0}{2\pi I_c}\hat{K}\hat{L}^{-1}\hat{D}\vec{\varphi} + \vec{C}\right], \quad (27)$$

where $\vec{C} = \left(\hat{K}_I^{-1}\vec{I}_b - \hat{K}\hat{L}^{-1}\vec{\Phi}_{nf}\right)/I_c$ is a vector with time-independent components. Equation (27) is the key equation of our paper.

D. Thermal noise and numerical method

To generate the individual thermal noise at each JJ, we use the approach used by Tesche and Clarke [6] and Voss [5]. The normalized noise currents are generated at each time step using random number generators that follow a Gaussian distribution, where the mean and mean-square deviation satisfy

$$\overline{i_{n,k}} = 0,$$
$$\overline{i_{n,k}^2} = 2\Gamma/\Delta\tau.$$

Here, Γ is the thermal-noise strength

$$\Gamma = \frac{2\pi k_B T}{\Phi_0 I_c}, \quad (28)$$

where k_B is the Boltzmann constant, T is the device operating temperature, and $\Delta\tau$ is the normalized time step used when solving Eq. (27) numerically. In this work, we use $T = 77$ K and $\Delta\tau = 0.1$.

We solve Eq. (27) using numerical integration; to do so, we must choose the initial conditions of the JJ phase differences $\varphi_k(0)$. We find that a good choice for the initial condition of the overdamped system of Eq. (27) is $\varphi_{1+N_p(n-1)}(0) = 0$ for the first JJ of each row n and

$$\varphi_{k+1}(0) = \varphi_k(0) + \frac{2\pi\Phi_s^a}{\Phi_0} \quad (29)$$

within each SQUID, where s is the SQUID index and $k = s + (n-1)$. The Euler method and Runge-Kutta fourth-order method are both tested and give convergent results. The data presented in this paper have been obtained using the Euler method, since it is computationally faster.

E. Voltage of 2D arrays

Once Eq. (27) is solved, we can integrate the second Josephson equation, i.e., $V_k(t) = (\Phi_0/2\pi)(\partial\varphi_k(t)/\partial t)$, to obtain the time-averaged voltage $\bar{V}_k$ at the kth JJ. Then, the normalized time-averaged voltage is $\bar{v}_k = \bar{V}_k/(I_cR)$.

The normalized time-averaged voltage $\bar{v}$ across the whole array, between the top and bottom leads, is given by

$$\bar{v} = \sum_{n=0}^{N_s-1}\frac{1}{N_p}\sum_{k=nN_p+1}^{(n+1)N_p}\bar{v}_k. \quad (30)$$

The time-averaged voltages across JJs in the same row are identical. Averaging over voltages in the same row as in Eq. (30) improves the numerical accuracy. In this work, 10^5 time iterations are needed to achieve a voltage numerical error of less than 1%. In case of the transfer function, which is the derivative of the voltage with respect to the applied flux, smoother voltage curves are needed in order to achieve sufficient accuracy. Thus, when calculating the transfer function, 10^6 time iterations are used.

III. SIMULATION, RESULTS, AND DISCUSSION

The time-averaged normalized voltage $\bar{v}$ of a (N_s, N_p) array with uniform bias-current injection depends on the parameter set $\{N_s, N_p, I_c, \tilde{L}, T, I_b, \vec{\Phi}_a\}$, where $\tilde{L}$ represents all the partial inductances. The parameter set is particularly large for SQIF arrays, where the SQUID loops have different sizes. The operating temperature T is taken as fixed, while I_b and $\vec{\Phi}_a$ depend on external sources and can be easily adjusted. The bias current I_b can be tuned to optimize the voltage-modulation depth, $\Delta\bar{v} = \max(\bar{v}) - \min(\bar{v})$, and $\vec{\Phi}_a$ can be adjusted to find the maximum transfer function $\bar{v}_\phi^{\max} = \max(\partial\bar{v}/\partial\phi)$ for a given I_b. $\bar{v}_\phi^{\max}$ can then be optimized by finding the optimal I_b. If only SQUID-loop self-inductances are important, the set of parameters for $\bar{v}_\phi^{\max}$ of a SQUID array reduces to $\{N_s, N_p, I_c, T, L_s, I_b, \Phi_a\}$,

where L_s is the SQUID-loop self-inductance. In this case, the alternative set $\{N_s, N_p, \beta_L, \Gamma, i_b, \phi_a\}$ can be used, where β_L is the screening parameter, $\beta_L = 2L_s I_c/\Phi_0$, and $i_b = I_b/I_c$. Using our partial-inductance matrices, the SQUID-loop self-inductance is defined as

$$L_s = 2\left(L_{11}^{v} + L_{11}^{H}\right). \tag{31}$$

In this study, we consider arrays with film thickness $d = 0.22$ μm, junction width $w = 2$ μm, London penetration depth $\lambda = 0.4$ μm, and bias lead lengths 100 μm and the device operating temperature is fixed at $T = 77$ K. Also, unless stated otherwise, we use square-SQUID loops $a_x = a_y = 10$ μm and a critical current of $I_c = 20$ μA as an example value, which is measured for HTS step-edge junctions [10,33]. These values give $\beta_L = 0.7$ and $\Gamma = 0.16$ [Eq. (28)]. In this paper, we calculate the inductance by assuming a homogeneous current density across the superconducting tracks. For the geometric partial inductances, we apply the analytical expressions derived by Hoer and Love [42]. If more accurate inductance calculations are needed in the case of wider tracks, we can obtain the inductances using finite-element methods such as 3D-MLSI [43] or FastHenry [44,45] and implement them in our model.

Our model shows excellent agreement with the analytical formula given by Oppenländer *et al.* [13] for 1D SQUID arrays, which is valid in the $\beta_L << 1$ limit.

A. The importance of thermal noise

Yttrium barium copper oxide (YBCO) step-edge JJs at $T = 77$ K have been shown to have a critical current of $I_c = 20$ μA [10,33] and thus $\Gamma = 0.16$. In our calculations, we can turn off the effect of the thermal noise by setting $\Gamma = 0$.

Figure 3(a) compares $\bar{v}(\phi_a)$ curves, where $\phi_a = \Phi_a/\Phi_0$, of a $(1, 11)$-SQUID array for $\Gamma = 0.16$ with curves for $\Gamma = 0$ at $i_b = 0.5$, 0.75 and 1. The $\bar{v}(\phi_a)$ of a 1D or 2D SQUID array is periodic in ϕ_a with period 1, as in the case of a symmetric dc SQUID. For $i_b < 1$, the dashed $\Gamma = 0$ curves show zero-voltage regions, while with thermal noise, the SQUID array is always in a nonzero-voltage state for $i_b > 0$. In Fig. 3(b), we show the corresponding transfer function $\bar{v}_\phi(\phi_a) = \partial\bar{v}(\phi_a)/\partial\phi_a$, which demonstrates that the inclusion of thermal noise is crucial in obtaining the correct transfer function. Also, it shows that the normalized bias current that optimizes the transfer function is smaller than one. Thus, it is essential to include the effect of thermal noise when calculating the behavior of 2D SQUID arrays at 77 K.

B. Voltage versus magnetic flux response of (N_s, N_p)-SQUID arrays

Figure 4 shows the N_s-normalized voltage $\bar{v}/N_s$ versus ϕ_a at 77 K using different i_b for four (N_s, N_p)-SQUID

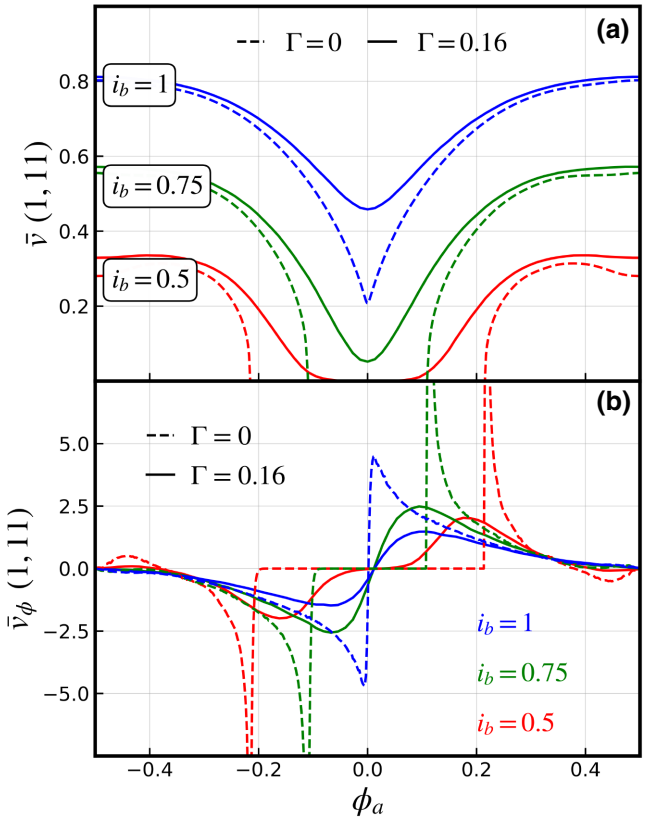

FIG. 3. (a) The time-averaged voltage $\bar{v}$ versus ϕ_a of a 1D SQUID array with $N_p = 11$ at three different bias currents i_b and thermal-noise strength $\Gamma = 0$ (dashed lines) and at $\Gamma = 0.16$ (solid lines). (b) The corresponding transfer function $\bar{v}_\phi$ versus ϕ_a.

arrays. Figure 4(a) depicts $(1, 2)$ and $(10, 2)$ SQUID arrays, while Fig. 4(b) shows $(1, 11)$ and $(10, 11)$ SQUID arrays. The solid curves belong to the short arrays (1D parallel arrays) with $N_s = 1$, while the dashed curves are the long arrays with $N_s = 10$. Figure 4 reveals the validity of the scaling approximation

$$\bar{v}(N_s, N_p) \approx N_s\ \bar{v}(1, N_p). \tag{32}$$

When comparing the dashed curves with the solid ones in Fig. 4, we can see that the scaling approximation given in Eq. (32) holds reasonably well for certain i_b and ϕ_a; in particular, for not too small i_b and ϕ_a values. Equation (32) holds very well for series arrays of dc SQUIDs and $(N_s, 2)$ arrays and reasonably well for 2D arrays $(N_s, 11)$ in the high-i_b and -ϕ_a regime [Fig. 4(b)]. We discuss the validity of the scaling approximation in more detail further below. Comparison of the $N_p = 2$ with the $N_p = 11$ curves shows that the wider arrays produce sharper voltage dips and thus the applied flux ϕ_a^* that maximizes the transfer function is smaller for the wider arrays.

Figure 5 illustrates the effect of considering the partial inductances of the whole array, labeled as "all partial

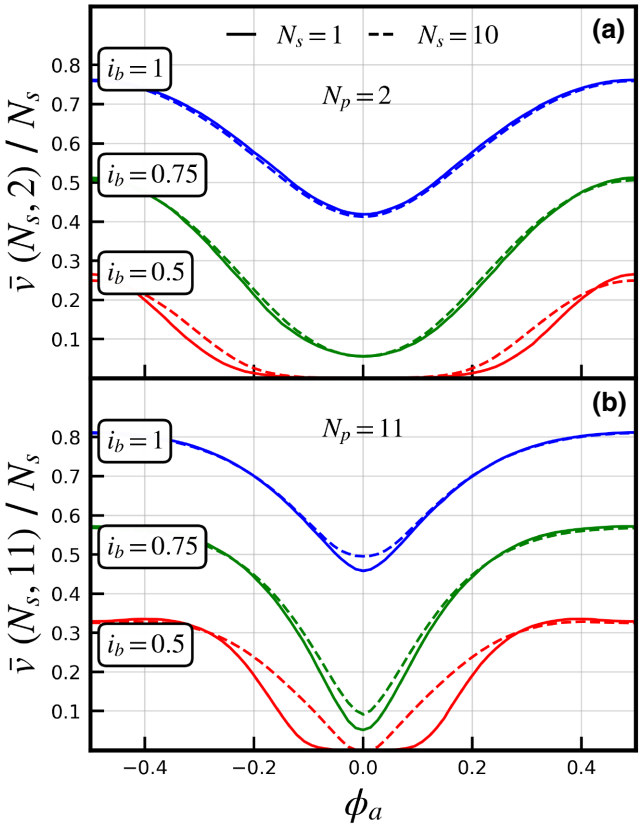

FIG. 4. The $\bar{v}/N_s$ versus ϕ_a for different bias currents i_b at $T = 77$ K: (a) $(N_s, 2)$-SQUID arrays; (b) $(N_s, 11)$-SQUID arrays. The solid lines represent 1D arrays ($N_s = 1$) and the dashed lines represent 2D arrays with $N_s = 10$. For these arrays, $\beta_L = 0.7$, $\Gamma = 0.16$.

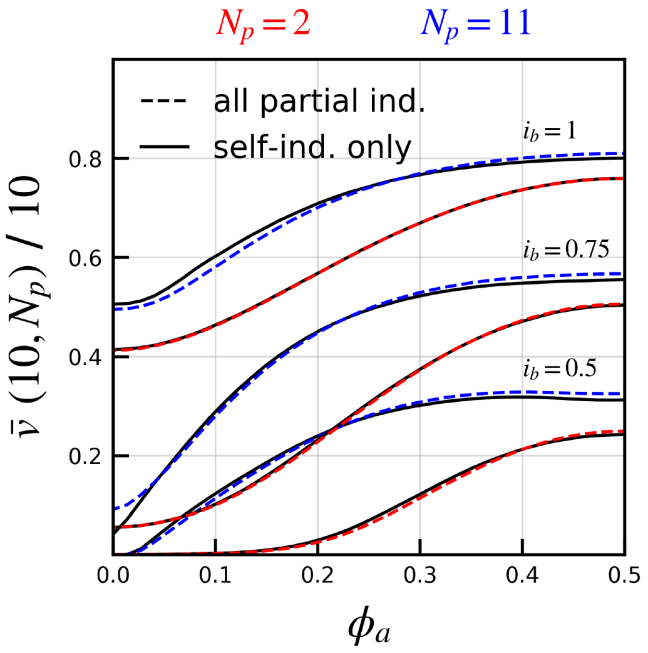

FIG. 5. $\bar{v}/N_s$ versus ϕ_a for $(10, N_p)$ arrays with $N_p = 2$ (red) and $N_p = 11$ (blue). The black solid curves are simulations considering only self-inductances, labeled "self-ind. only," while the dashed curves take into account the partial inductances of the whole array and are labeled "all partial ind." For these arrays, $\beta_L = 0.7$, $\Gamma = 0.16$.

ind." (dashed lines), versus the response where only the self-inductance contributions are considered, labeled "self-ind.only" (black solid lines). In our case, "self-ind. only" means that when calculating the flux inside a loop area, we only take into account the four partial inductances that are part of that loop. Here, we study $(10, N_p)$-SQUID arrays with $N_p = 2$ and $N_p = 11$ at three different i_b, with $\beta_L = 0.7$ and $\Gamma = 0.16$. Only minor differences are noticeable for the overall voltage response. Interestingly, Dalichaouch *et al.* [36] have claimed that considering the inductance contributions of the whole array is important in order to obtain the correct transfer function and voltage response but their calculations have been done without thermal noise at $\Gamma = 0$.

The relative difference between the voltage-to-flux response for "self-ind. only" and "all partial ind." can become significant for large β_L. However, it depends on the values chosen for the critical current and SQUID-loop size. For instance, fixing $a_x = a_y = 10$ μm and increasing β_L by increasing I_c will increase the relative difference, particularly around the minima of the $\bar{v}(\phi_a)$ curves. On the other hand, fixing $I_c = 20$ μA and increasing β_L by increasing the SQUID-loop size a_x will not show an increase in the relative difference.

The difference in the voltage-to-flux response between "self-ind. only" and "all partial ind." seen in Fig. 5 is reduced compared to the difference that we would observe in a model in which the mutual inductances, defined by circulating loop currents, could be turned on or off.

The computational time needed for our simulations does not increase significantly when the partial inductances of the whole array are included and therefore the simulations presented in this paper consider all the partial inductances of the array.

C. Maximum transfer-function dependence on the bias current

In Fig. 6, we show the normalized maximum transfer function $\bar{v}_\phi^{\max}/N_s = \bar{v}(\phi_a^*, i_b)/N_s$ versus the bias current, $i_b = I_b/I_c$, for six different (N_s, N_p)-SQUID arrays operating at $T = 77$ K. The solid lines with diamond symbols correspond to 1D SQUID arrays and the dashed lines with circles describe 2D SQUID arrays with $N_s = 10$. The colors describe the number of junctions in parallel of each array, i.e., red for $N_p = 2$, green for $N_p = 5$, and blue for $N_p = 11$. From Fig. 6, we can see that an optimal bias current i_b^* exists for each array with $i_b^* \approx 0.75$. Figure 6 also reveals that while $\bar{v}_\phi^{\max}$ is obtained at slightly different

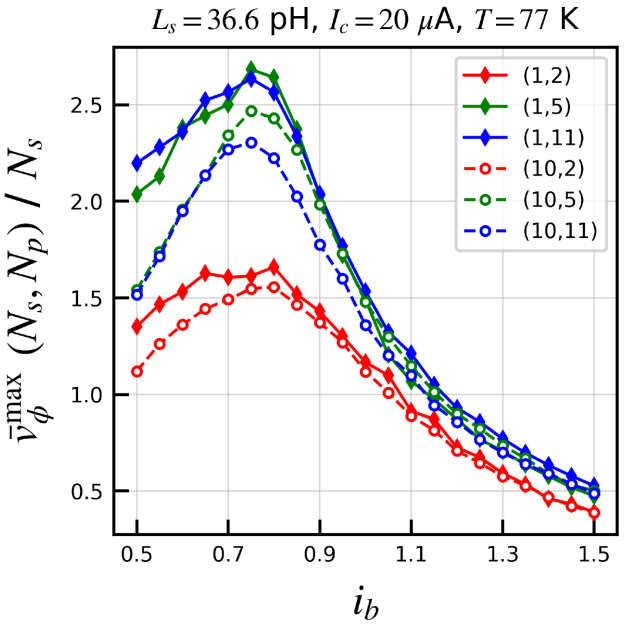

FIG. 6. The normalized maximum transfer function $\bar{v}_\phi^{\max}/N_s$ versus the bias current i_b at $T = 77$ K for six different SQUID arrays, i.e., three 1D arrays (solid lines with diamond symbols) and three 2D arrays with $N_s = 10$ (dashed lines with circles). The colors indicate the number of JJs in parallel: $N_p = 2$ (red), $N_p = 5$ (green), and $N_p = 11$ (blue).

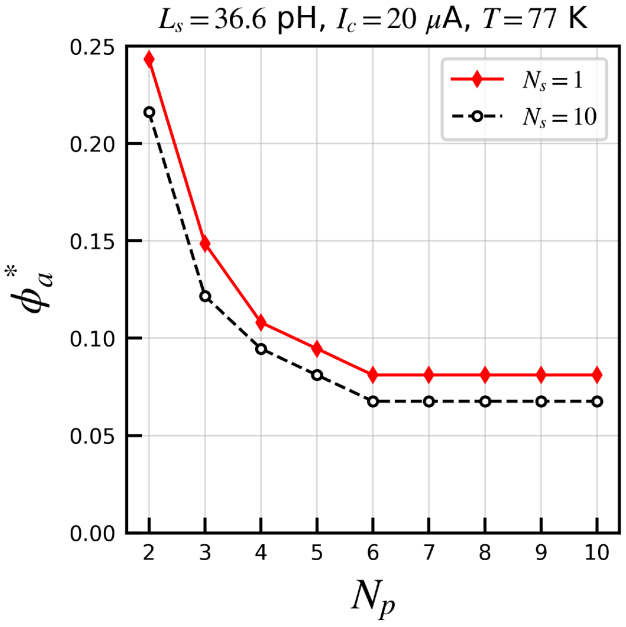

FIG. 7. The applied magnetic flux ϕ_a^* that maximizes $\bar{v}_\phi$ versus N_p for $(1, N_p)$-SQUID arrays (solid lines with diamonds) and $(10, N_p)$-SQUID arrays (dashed lines with circles) at 77 K for the bias current $i_b = 0.75$, which is near the i_b^* value of each array.

values of ϕ_a and i_b for different N_s, it satisfies the scaling approximation [Eq. (32)] within about 20% at bias currents close to the i_b^* value. This can be seen by comparing open and solid symbols for the same colored curves. For larger bias currents the maximum transfer functions scale very well with N_s for all N_p studied. Figure 6 further shows a significant increase of $\bar{v}_\phi^{\max}/N_s$ from $N_p = 2$ to $N_p = 5$. This is due to the sharpening of the dip of $\bar{v}(\phi_a)$ with N_p, which can also be seen in Fig. 4 by comparing the $N_p = 2$ arrays with the $N_p = 11$ ones. This effect has previously been reported by Oppenländer *et al.* [13] for uniformly biased SQIF arrays at $T = 0$ K. While in Fig. 6 there is a large difference between $N_p = 2$ and $N_p = 5$, this is not the case for $N_p = 5$ and $N_p = 11$. The reason for this is discussed below.

The optimal applied magnetic flux ϕ_a^* that maximizes the transfer function $\partial\bar{v}/\partial\phi_a$ at $i_b = 0.75$, which is close to the i_b^* of each array, is shown in Fig. 7 as a function of N_p for $N_s = 1$ and 10. While $\phi_a^* \approx 0.25$ for a single dc SQUID and dc SQUIDs in series, ϕ_a^* drops to $\phi_a^* \approx 0.07$ for wider arrays with $N_p \geq 5$. There is not much difference in ϕ_a^* for $N_s = 1$ and $N_s = 10$.

D. Maximum transfer-function dependence on critical current and SQUID self-inductance

In Sec. III B, we see that for these kinds of arrays, only self-inductance contributions are of importance and therefore either L_s and T together with I_c or β_L and Γ can be used as array parameters.

Figure 8 shows the normalized maximum transfer function $\bar{v}_\phi^{\max}/N_s$ versus i_b depending on β_L and Γ for different (N_s, N_p)-SQUID arrays. The line colors represent the different β_L values: in cyan, $\beta_L = 0.02$; in magenta, $\beta_L = 0.18$; in red, $\beta_L = 0.35$; in blue, $\beta_L = 0.7$; and in green, $\beta_L = 1.4$. The solid lines describe 1D arrays, $N_s = 1$, while the dashed lines are used for 2D arrays with $N_s = 10$. Figures 8(a) and 8(b) illustrate the dependence of $\bar{v}_\phi^{\max}(i_b)/N_s$ on the SQUID-loop self-inductance L_s for a fixed $I_c = 20$ μA ($\Gamma = 0.16$). On the other hand, in Figs. 8(c)–8(f) we show $\bar{v}_\phi^{\max}/N_s$ versus i_b for arrays with different I_c with a fixed $L_s = 36.6$ pH, which corresponds to a SQUID-loop size of $a_x = a_y = 10$ μm. Figures 8(a), 8(c) and 8(e) illustrate $(N_s, 2)$-SQUID arrays, while Figs. 8(b), 8(d), and 8(f) show $(N_s, 11)$-SQUID arrays.

By comparing solid and dashed lines, Fig. 8 reveals that the scaling approximation given in Eq. (32) holds very well for all the arrays and β_L and Γ values shown here, especially for dc SQUIDs in series ($N_p = 2$). Also, the approximation holds best for $i_b \geq i_b^*$.

From Figs. 8(a) and 8(b), we can see that $\bar{v}_\phi^{\max}(i_b)/N_s$ increases with decreasing SQUID-loop self-inductance L_s and therefore β_L. Figures 8(c) and 8(d) show that the maximum transfer function $\bar{v}_\phi^{\max}$ of the $(N_s, 2)$ and $(N_s, 11)$ arrays initially increases with decreasing I_c. This is because β_L decreases and the effect of thermal noise is still small. But as I_c decreases further, below the optimal critical

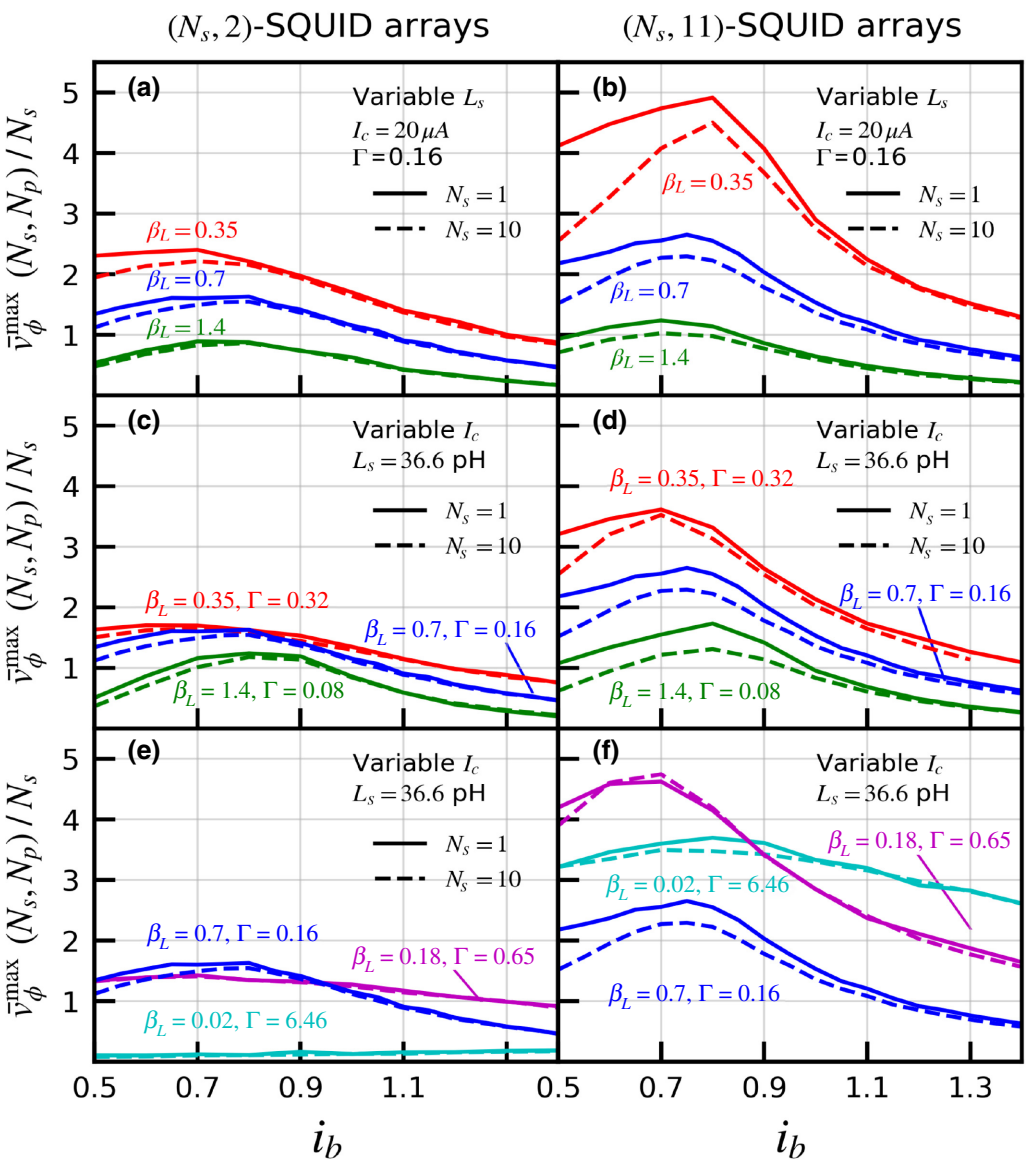

FIG. 8. The normalized maximum transfer function $\bar{v}_\phi^{\max}/N_s$ versus the bias current i_b at $T = 77$ K of 1D SQUID arrays (solid lines) and 2D SQUID arrays (dashed lines): (a),(c),(e) $(N_s, 2)$-SQUID arrays; (b), (d),(f) $(N_s, 11)$-SQUID arrays. (a),(b) Arrays with different SQUID self-inductances L_s. The JJ critical current is fixed at $I_c = 20\,\mu$A ($\Gamma = 0.16$). In red, $\beta_L = 0.35$ ($L_s = 18.1$ pH); in blue, $\beta_L = 0.7$ ($L_s = 36.6$ pH); and in green, $\beta_L = 1.4$ ($L_s = 72.5$ pH). (c),(d),(e),(f) Arrays with different critical currents I_c. The SQUID self-inductance is fixed at $L_s = 36.6$ pH. In cyan, $\beta_L = 0.02$, $\Gamma = 6.46$ ($I_c = 0.5\ \mu$A); in magenta, $\beta_L = 0.18$, $\Gamma = 0.65$ ($I_c = 5\ \mu$A); in red, $\beta_L = 0.35$, $\Gamma = 0.32$ ($I_c = 10\,\mu$A); in blue, $\beta_L = 0.7$, $\Gamma = 0.16$ ($I_c = 20\ \mu$A); and in green, $\beta_L = 1.4$, $\Gamma = 0.08$ ($I_c = 40\ \mu$A).

current I_c^*, the $\bar{v}_\phi^{\max}$ starts to decrease, as can be seen in Figs. 8(e) and 8(f). For $I_c \le I_c^*$, the benefit of a small β_L diminishes as the large thermal-noise strength $\Gamma = 2\pi k_B T/(\Phi_0 Ic)$ flattens the flux-to-voltage response curve. We find, for $L_s = 36.6$ pH, that the optimal critical current I_c^* of the $(N_s, 2)$-SQUID array is $I_c^* \approx 20\ \mu$A, which can be estimated from $\Gamma = \beta_L$, while for $(N_s, 11)$, we find that $I_c^* \approx 2\ \mu$A.

E. Maximum transfer-function dependence on N_s, N_p, and the coupling radius

To better understand the dependence of the maximum transfer function $\bar{v}_\phi^{\max}$ on the array dimensions, N_s and N_p, at $T = 77$ K, we show in Fig. 9 a 3D plot using a bias current of $i_b = 0.75$, which is close to the optimal bias current for most arrays. Figure 9 clearly shows that the maximum transfer function depends linearly on N_s. In contrast, $\bar{v}_\phi^{\max}$ initially increases with N_p up to $N_p^* \approx 3.5$, followed by a small decrease and a plateau for larger N_p. N_p^* does not depend on N_s. This plateauing behavior has previously been reported for 1D parallel array calculations at $T = 0$ K by Kornev *et al.* [27,28] and also experimentally and theoretically by Mitchell *et al.* [10]. Kornev *et al.* [27,28] have explained this behavior using the concept of a "coupling radius" (or "interaction radius") N_p^*, which arises because the array acts as an *RL* network, which, depending on its operating frequency, only allows N_p^* parallel JJs to couple or interact. According to Kornev *et al.* [28], N_p^* depends on the normalized coupling impedance ωl of the array, which can be expressed as $\omega l = \pi \beta_L \bar{v}(\phi_a^*, i_b^*)$.

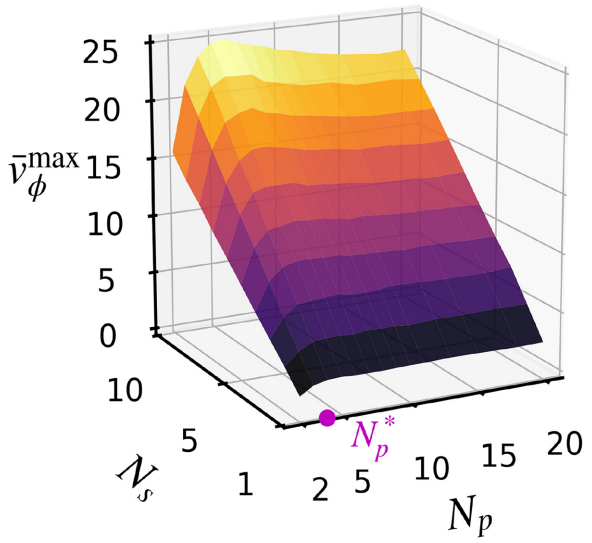

FIG. 9. The maximum transfer function $\bar{v}_\phi^{\max}$ versus N_s and N_p at $T = 77$ K for a bias current $i_b = 0.75$. The SQUID arrays have square SQUID loops, i.e., $a_x = a_y = 10$ μm ($L_s = 36.6$ pH), $I_c = 20$ μA ($\beta_L = 0.7$ and $\Gamma = 0.16$), and $N_p^* \approx 3.5$, marked with a magenta circle.

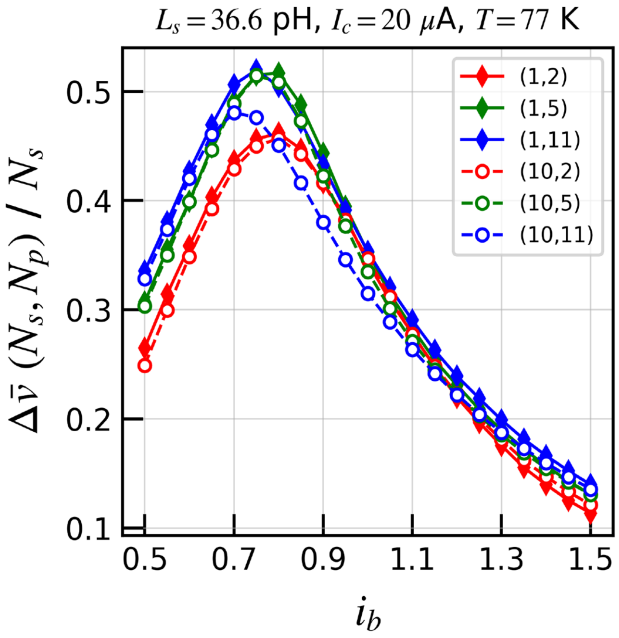

FIG. 10. The normalized voltage-modulation depth $\Delta\bar{v}/N_s$ versus the bias current i_b at $T = 77$ K for three 1D arrays (solid lines with diamonds) and three 2D arrays with $N_s = 10$ (dashed lines with circles). The colors indicate the number of JJs in parallel: $N_p = 2$ (red), $N_p = 5$ (green), and $N_p = 11$ (blue).

For the optimal transfer function $\bar{v}_\phi(N_s, N_p, \phi_a^*, i_b^*)$ we find from our simulations that

$$\bar{v}_\phi(N_s, N_p, \phi_a^*, i_b^*) \approx \frac{N_s \tilde{N}_p}{2}\, \bar{v}_\phi(1, 2, \phi_a^*, i_b^*). \tag{33}$$

Here, $\bar{v}_\phi(1, 2, \phi_a^*, i_b^*)$ is the optimal transfer function of the dc-SQUID cell and $\tilde{N}_p = N_p$ if $N_p < N_p^*$ and $\tilde{N}_p = N_p^*$ otherwise. N_p^* is the so-called array coupling radius. N_p^* increases with decreasing normalized inductive reactance of the SQUID loop [28]. It is also important to note that the optimal values ϕ_a^* and i_b^* of a single SQUID are not the same as the optimal values for an arbitrary (N_s, N_p)-SQUID array. We test numerically the validity of the scaling behavior of Eq. (33) in the parameter range $0.1 \le \beta_L \le 2$ and $0.03 \le \Gamma \le 1$ and find Eq. (33) to be accurate within 25%.

The scaling behavior shown in Eq. (33) can also be seen in Fig. 8 by comparing the dc SQUIDs [Figs. 8(a), 8(c) and 8(e)] with the $(N_s, 11)$-SQUID arrays [Figs. 8(b), 8(d) and 8(f)].

F. Voltage-modulation depth dependence on bias current

In Fig. 10, we study the same arrays as in Fig. 6(a) but in this case, instead of the $\bar{v}_\phi^{\max}$ we analyze the normalized voltage-modulation depth $\Delta\bar{v}/N_s = (\max(\bar{v}) - \min(\bar{v}))/N_s$ versus the bias current $i_b = I_b/I_c$ operating at $T = 77$ K. The solid lines with diamond symbols correspond to 1D SQUID arrays and the dashed lines with circles describe 2D SQUID arrays with $N_s = 10$. The colors indicate the number of JJs in parallel, i.e., red for $N_p = 2$, green for $N_p = 5$, and blue for $N_p = 11$. From Fig. 10, we can see that an optimal bias current i_b^* exists for each array, with $i_b^* \approx 0.7 - 0.8$. We can further see that also $\Delta\bar{v}$ satisfies the scaling approximation in Eq. (32) very well for $N_p = 2$ and $N_p = 5$. For $N_p = 11$, the scaling approximation holds within 10% in the region close to i_b^*. The optimal bias current for $N_p = 11$ is slightly different between the 1D and 2D arrays, being $i_b^* \approx 0.7$ for the 2D array and $i_b^* \approx 0.75$ for the 1D array.

Comparison of Fig. 6(a) with Fig. 10 reveals that the i_b^* values for $\Delta\bar{v}/N_s$ and for $\bar{v}_\phi^{\max}/N_s$ are very similar and therefore experimentally we could use the maximum voltage-modulation depth to obtain the optimal bias current of the maximum transfer function.

G. Voltage versus magnetic flux response of (N_s, N_p)-SQIF arrays

For some applications, such as absolute field magnetometers [23], the periodicity of the $\bar{v}(\phi_a)$ response of dc SQUIDs and SQUID arrays is not a desirable feature, since it does not offer a unique response. For these kind of applications, SQIF arrays are preferred because the periodicity with the magnetic flux is broken by introducing a spread in the SQUID-loop areas of the array. The array structures considered in our model follow gridlike patterns. This kind of structure implies that SQUIDs in the same row must have the same height and SQUIDs in the same column

must have the same width (see Fig. 1). With these two restrictions in mind, we can create a SQIF response by changing the width and/or height of the SQUID loops.

In Fig. 11(a), we show the voltage $\bar{v}$ versus the averaged magnetic flux $\langle\phi_a\rangle = \sum_{s=1}^{N_{SQ}} \phi_s^a / N_{SQ}$ of five different SQIF arrays at $T = 77$ K and $i_b = 1$. All these arrays have 11 junctions in parallel ($N_p = 11$) and the colors of the curves indicate the number of SQUIDs in series, with $N_s = 1$ (red), $N_s = 3$ (blue), and $N_s = 5$ (green). The SQIFs represented with dashed lines are created by only varying the width a_x of the SQUIDs using random normally distributed values, with a standard deviation of approximately 30%. The 2D SQIFs ($N_s = 3$ and $N_s = 5$) represented with solid lines are obtained by adding an approximately 30% spread in the height a_y of the SQUIDs. Figure 11(a) shows that the SQIFs with spreads in both directions have less prominent secondary peaks than the SQIFs with spread only in a_x. The modulation depth of the main dip gets slightly reduced for spreads in both a_x and a_y.

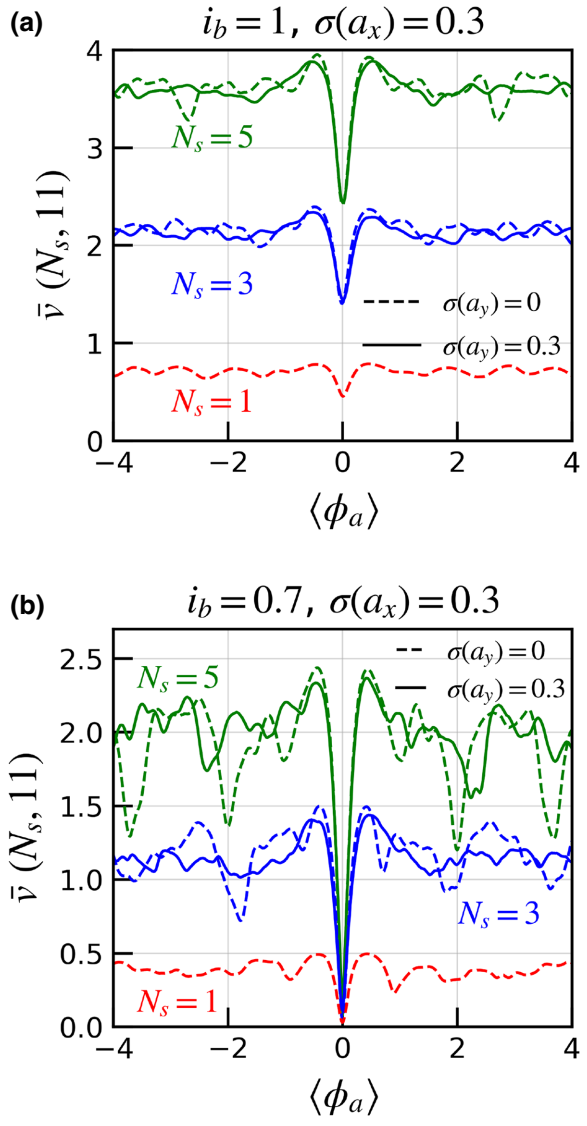

FIG. 11. The time-averaged voltage $\bar{v}$ dependence on the averaged normalized applied magnetic flux $\langle\phi_a\rangle$ of SQIF arrays with $N_p = 11$ for different N_s: in red, the 1D SQIF; in blue, the 2D SQIF with $N_s = 3$; and in green, the 2D SQIF with $N_s = 5$. The dashed lines represent SQIF arrays with only an a_x spread, $\sigma(a_x) = 0.3$, while the solid lines show 2D SQIFs with spreads in a_x and a_y. The SQUID mean sizes are $\langle a_x\rangle = \langle a_y\rangle = 10\ \mu$m, $T = 77$ K and the bias current is (a) $i_b = 1$ and (b) $i_b = 0.7$.

Figure 11(b) shows $\bar{v}$ versus $\langle\phi_a\rangle$ for $i_b = 0.7$, close to the optimal i_b^* value. We can see that the voltage-modulation depths of the main dip of the SQIF arrays in Fig. 11(b) are larger than those of Fig. 11(a), where the bias current is $i_b = 1$.

In Fig. 11(b), we can see more clearly the effects of considering loop-area spreads in both a_x and a_y. By adding the spread in the loop width of each column and in the loop height of each row, we achieve a larger spread in the SQUID-loop areas, which creates stronger destructive interference.

Instead of generating SQIF arrays using randomly generated spreads with a given mean value, we could generate the SQUID loops in a systematic manner. One choice, which has been used before for 1D SQIF arrays [13], is to use Gaussian arrays to determine the height of each row and the width of each column. A systematic method would further reduce the secondary peaks, since it would ensure distinct SQUID-loop areas. It also could help to achieve greater linearity of $\bar{v}(\phi_a)$ around ϕ_a^* [19].

IV. SUMMARY

In this paper, we present a theoretical model that describes the behavior of 1D and 2D SQUID and SQIF arrays for uniform bias-current injection at $T = 77$ K. Besides the parameters that characterize a single dc SQUID, here the number N_s of SQUID rows and the number N_p of JJs in parallel, as well as the inductive coupling between SQUID loops, become additional parameters. The largest array size that we study is $(N_s, N_p) = (10, 11)$.

Our results show that the inclusion of Johnson thermal noise is paramount for correctly predicting the voltage response and the maximum transfer function. By comparing calculations with only self-inductances against simulations where the partial inductances of the whole array are considered, we elucidate the role of the inductive coupling between SQUID loops, revealing that the response for these kind of arrays is mainly defined by the self-inductance terms.

Furthermore, our simulations establish the validity of an approximate scaling behavior for the voltage in the form $\bar{v}(N_s, N_p) \approx N_s\ \bar{v}(1, N_p)$ for certain bias currents and applied fluxes [see Eq. (32)]. Such an approximate scaling is also found for the maximum transfer function and is most accurate for narrow arrays and large bias currents.

The applied magnetic flux that maximizes the transfer function is found to decrease with increasing N_p.

We demonstrate that the maximum transfer function can be optimized with a bias current $i_b^* = 0.7$–0.8. The optimal bias current is shown to depend only weakly on our choice of the SQUID self-inductance and JJ critical current.

Most importantly, our simulations reveal that the maximum transfer function of a 2D SQUID array is proportional to the maximum transfer function of the corresponding dc SQUID and scales with $N_s N_p/2$ or $N_s N_p^*/2$, where N_p^* is the so-called coupling radius, as shown in Eq. (33).

Our calculations also show that the bias current that optimizes the maximum transfer function also approximately optimizes the voltage-modulation depth of 2D SQUID arrays.

In addition, we study 2D SQIF arrays, where we compare arrays that only have a spread in the SQUID-loop height with arrays with spreads in both the SQUID-loop height and width. We show that increasing the spread in both directions further reduces secondary oscillations in the voltage response.

Our work offers researchers a theoretical model that can accurately simulate 1D and 2D SQUID and SQIF arrays made from HTS materials, as it fully includes thermal noise. The model could be used in the future to further deepen our understanding of the complicated parameter dependence of 2D SQUID and SQIF arrays.

[1] J. Clarke and A. I. Braginski, *Materials and Manufacturing Processes*, edited by John Clarke and Alex I. Braginski (Wiley, 2004), Vol. 1.

[2] J. R. Clem and E. H. Brandt, Response of thin-film SQUIDs to applied fields and vortex fields: Linear SQUIDs, Phys. Rev. B **72**, 174511 (2005).

[3] C. P. Foley *et al.*, Field trials using HTS SQUID magnetometers for ground-based and airborne geophysical applications, IEEE Trans. Appl. Supercond. **9**, 3786 (1999).

[4] V. Ambegaokar and B. I. Halperin, Voltage due to thermal noise in the dc Josephson effect, Phys. Rev. L **22**, 1364 (1969).

[5] R. F. Voss, Noise characteristics of an ideal shunted Josephson junction, J. Low. Temp. Phys. **42**, 151 (1981).

[6] C. D. Tesche and J. Clarke, dc SQUID: Noise and optimization, J. Low. Temp. Phys. **29**, 301 (1977).

[7] K. Enpuku, Y. Shimomura, and T. Kisu, Effect of thermal noise on the characteristics of a high T_c superconducting quantum interference device, J. Appl. Phys. **73**, 7929 (1993).

[8] J. H. Miller, G. H. Gunaratne, J. Huang, and T. D. Golding, Enhanced quantum interference effects in parallel Josephson junction arrays, Appl. Phys. Lett. **59**, 3330 (1991).

[9] R. Gerdemann, L. Alff, A. Beck, O. M. Froehlich, B. Mayer, and R. Gross, Josephson vortex-flow transistors based on parallel arrays of $YBa_2Cu_3O_{7-\delta}$ bicrystal grain boundary junctions, IEEE Trans. Appl. Supercond. **5**, 3292 (1995).

[10] E. E. Mitchell, K. H. Müller, W. E. Purches, S. T. Keenan, C. J. Lewis, and C. P. Foley, Quantum interference effects in 1D parallel high-T_c SQUID arrays with finite inductance, Supercond. Sci. Technol. **32**, 124002 (2019).

[11] V. Foglietti, K. G. Stawiasz, M. B. Ketchen, and R. H. Koch, Performance of a flux locked series SQUID array, IEEE Trans. Appl. Supercond. **3**, 3061 (1993).

[12] S. Krey, O. Brugmann, H. Burkhardt, and M. Schilling, Noise properties of $YBa_2Cu_3O_7$ Josephson junction array magnetometers, IEEE Trans. Appl. Supercond. **9**, 3401 (1999).

[13] J. Oppenländer, Ch. Häussler, and N. Schopohl, Non-Φ_0-periodic macroscopic quantum interference in one-dimensional parallel Josephson junction arrays with unconventional grating structure, Phys. Rev. B **63**, 024511 (2000).

[14] Ch. Häussler, J. Oppenländer, and N. Schopohl, Nonperiodic flux to voltage conversion of series arrays of dc superconducting quantum interference devices, J. Appl. Phys. **89**, 1875 (2001).

[15] J. Oppenlander, T. Trauble, C. Haussler, and N. Schopohl, Superconducting multiple loop quantum interferometers, IEEE Trans. Appl. Supercond. **11**, 1271 (2001).

[16] J. Oppenländer, Ch. Häussler, T. Träuble, and N. Schopohl, Highly sensitive magnetometers for absolute magnetic field measurements based on quantum interference filters, Phys. C: Supercond. **368**, 119 (2002).

[17] J. Oppenlander, Ch. Haussler, T. Trauble, P. Caputo, J. Tomes, A. Friesch, and N. Schopohl, Two dimensional superconducting quantum interference filters, IEEE Trans. Appl. Supercond. **13**, 771 (2003).

[18] V. K. Kornev, I. I. Soloviev, J. Oppenlaender, Ch. Haeussler, and N. Schopohl, The oscillation linewidth and noise characteristics of a parallel superconducting quantum interference filter, Supercond. Sci. Technol. **17**, S406 (2004).

[19] V. K. Kornev, I. I. Soloviev, N. V. Klenov, and O. A. Mukhanov, High linearity SQIF-like Josephson-junction structures, IEEE Trans. Appl. Supercond. **19**, 741 (2009).

[20] V. Schultze, R. IJsselsteijn, R. Boucher, H.-G. Meyer, J. Oppenländer, Ch. Häußler, and N. Schopohl, Improved high-T_c superconducting quantum interference filters for sensitive magnetometry, Supercond. Sci. Technol. **16**, 1356 (2003).

[21] J. Oppenländer, P. Caputo, Ch. Häussler, T. Träuble, J. Tomes, A. Friesch, and N. Schopohl, Effects of magnetic field on two-dimensional superconducting quantum interference filters, Appl. Phys. Lett. **83**, 969 (2003).

[22] P. Caputo, J. Oppenländer, Ch Häussler, J. Tomes, A. Friesch, T. Träuble, and N. Schopohl, High-performance magnetic field sensor based on superconducting quantum interference filters, Appl. Phys. Lett. **85**, 1389 (2004).

[23] P. Caputo, J. Tomes, J. Oppenlander, C. Haussler, A. Friesch, T. Trauble, and N. Schopohl, Superconducting quantum interference filters as absolute magnetic field sensors, IEEE Trans. Appl. Supercond. **15**, 1044 (2005).

[24] V. Schultze, R. IJsselsteijn, and H.-G. Meyer, How to puzzle out a good high-T_c superconducting quantum interference filter, Supercond. Sci. Technol. **19**, S411 (2006).

[25] P. Caputo, J. Tomes, J. Oppenländer, Ch. Häussler, A. Friesch, T. Träuble, and N. Schopohl, Quadratic mixing of radio frequency signals using superconducting quantum interference filters, Appl. Phys. Lett. **89**, 062507 (2006).

[26] A. K. Kalabukhov, M. L. Chukharkin, A. A. Deleniv, D. Winkler, I. A. Volkov, and O. V. Snigirev, Analysis of the possibility to amplify an rf signal with a superconducting quantum interference filter, J. Commun. Technol. Electron. **53**, 934 (2008).

[27] V. K. Kornev, I. I. Soloviev, N. V. Klenov, T. V. Filippov, H. Engseth, and O. A. Mukhanov, Performance advantages and design issues of SQIFs for microwave applications, IEEE Trans. Appl. Supercond. **19**, 916 (2009).

[28] V. K. Kornev, I. I. Soloviev, N. V. Klenov, and O. A. Mukhanov, Design and experimental evaluation of SQIF arrays with linear voltage response, IEEE Trans. Appl. Supercond. **21**, 394 (2011).

[29] P. Longhini, S. Berggren, A. Palacios, V. In, and A. Leese de Escobar, Modeling non-locally coupled dc SQUID arrays, IEEE Trans. Appl. Supercond. **21**, 391 (2011).

[30] S. Berggren, Ph.D. thesis, Computational Science, Claremont Graduate University; San Diego State University, 2012.

[31] S. Berggren and A. Leese de Escobar, Effects of spread in critical currents for series- and parallel-coupled arrays of SQUIDs and bi-SQUIDs, IEEE Trans. Appl. Supercond. **25**, 1600304 (2015).

[32] K.-H. Müller and E. E. Mitchell, Theoretical model for parallel SQUID arrays with fluxoid focusing, Phys. Rev. B **103**, 054509 (2021).

[33] E. E. Mitchell, K. E. Hannam, J. Lazar, K. E. Leslie, C. J. Lewis, A. Grancea, S. T. Keenan, S. K. H. Lam, and C. P. Foley, 2D SQIF arrays using 20 000 YBCO high R_n Josephson junctions, Supercond. Sci. Technol. **29**, 06LT01 (2016).

[34] B. J. Taylor, S. A. E. Berggren, M. C. O'Brien, M. C. DeAndrade, B. A. Higa, and A. M. Leese de Escobar, Characterization of large two-dimensional $YBa_2Cu_3O_{7-\delta}$ SQUID arrays, Supercond. Sci. Technol. **29**, 084003 (2016).

[35] S. A. Cybart, T. N. Dalichaouch, S. M. Wu, S. M. Anton, J. A. Drisko, J. M. Parker, B. D. Harteneck, and R. C. Dynes, Comparison of measurements and simulations of series-parallel incommensurate area superconducting quantum interference device arrays fabricated from $YBa_2Cu_3O_{7-\delta}$ ion damage Josephson junctions, J. Appl. Phys. **112**, 063911 (2012).

[36] T. N. Dalichaouch, S. A. Cybart, and R. C. Dynes, The effects of mutual inductances in two-dimensional arrays of Josephson junctions, Supercond. Sci. Technol. **27**, 065006 (2014).

[37] S. K. Tolpygo and M. Gurvitch, Critical currents and Josephson penetration depth in planar thin-film high-T_c Josephson junctions, Appl. Phys. Lett. **69**, 3914 (1996).

[38] R. S. Newrock, C. J. Lobb, U. Geigenmüller, and M. Octavio, in *Solid State Physics—Advances in Research and Applications* (2000), Vol. 54, p. 263.

[39] M. Tinkham, *Introduction to Superconductivity* (Dover Publications, New York, 2004), 2nd ed.

[40] F. London and H. London, The electromagnetic equations of the supraconductor, Proc. R. Soc. London, Ser. A—Math. Phys. Sci. **149**, 71 (1935).

[41] J. Pearl, Current distribution in superconducting films carrying quantized fluxoids, Appl. Phys. Lett. **5**, 65 (1964).

[42] C. Hoer and C. Love, Exact inductance equations for rectangular conductors with applications to more complicated geometries, J. Res. Natl. Bur. Standards, Sect. C: Eng. Instrum. **69C**, 127 (1965).

[43] M. M. Khapaev, A. Yu. Kidiyarova-Shevchenko, P. Magnelind, and M. Yu. Kupriyanov, 3D-MLSI: Software package for inductance calculation in multilayer superconducting integrated circuits, IEEE Trans. Appl. Supercond. **11**, 1090 (2001).

[44] M. Kamon, M. J. Ttsuk, and J. K. White, FastHenry: A multipole-accelerated 3-D inductance extraction program, IEEE Trans. Microw. Theory Tech. **42**, 1750 (1994).

[45] J. Tausch and J. White, Capacitance extraction of 3-D conductor systems in dielectric media with high-permittivity ratios, IEEE Trans. Microw. Theory Tech. **47**, 18 (1999).